IEEE Photonics Journal
An IEEE Photonics Society Publication

Open Access

Pixel-Reassigned Spectral-Domain Optical Coherence Tomography

Volume 10, Number 2, April 2018

En Bo
Lulu Wang
Jun Xie
Xin Ge
Linbo Liu

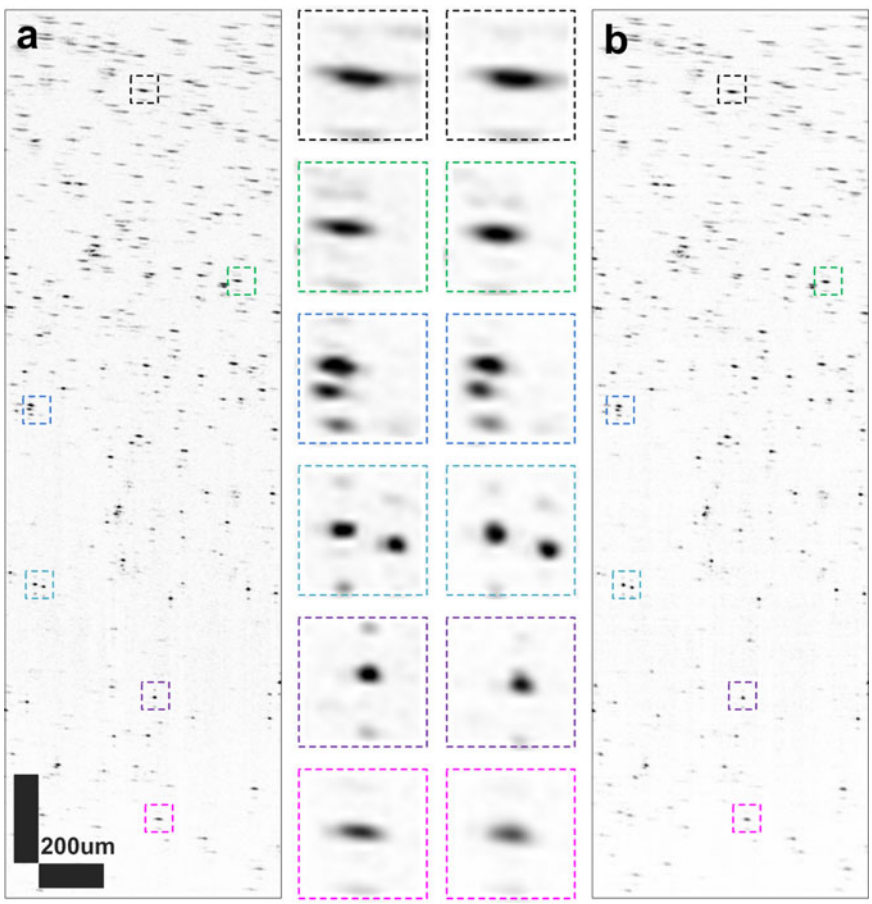

DOI: 10.1109/JPHOT.2018.2813523
1943-0655 © 2018 IEEE

IEEE photonics SOCIETY
IEEE

Pixel-Reassigned Spectral-Domain Optical Coherence Tomography

En Bo,[1] **Lulu Wang**,[1] **Jun Xie**,[1] **Xin Ge**,[1] **and Linbo Liu** [1,2]

[1]School of Electrical and Electronic Engineering, Nanyang Technological University, Singapore 639798
[2]School of Chemical and Biomedical Engineering, Nanyang Technological University, Singapore 637459

DOI:10.1109/JPHOT.2018.2813523

Manuscript received November 24, 2017; accepted March 5, 2018. Date of publication March 8, 2018; date of current version March 29, 2018.This work was supported in part by the National Research Foundation Singapore (NRF) (NRF-CRP13-2014-05); Ministry of Education Singapore (MOE2013-T2-2-107); National Medical Research Council Singapore (NMRC/CBRG/0036/2013); Nanyang Technological University-the Austrian Institute of Technology-the Medical University of Vienna (NTU-AIT-MUV) Program in Advanced Biomedical Imaging (NAM/15005). Corresponding author: Xin Ge and Linbo Liu (e-mail: gexin@ntu.edu.sg; liulinbo@ntu.edu.sg).

Abstract: A novel method of pixel reassignment (PRA) is proposed to achieve transverse superresolution in the confocal microscopy. Inspired by it, for the first time, we report a pixel-reassigned spectral-domain optical coherence tomography (OCT) with ~1.5 times transverse resolution improvement both in numerical simulations and imaging experiments. PRA is implemented by transversely shifting the detection fiber from the on-axis position to five off-axis positions, capturing cross-sectional images at each shifting step of the detection fiber and digitally reassigning them together to give a sharper image with moderately extended depth of focus and enhanced intensity. So, we believe that the PRA technique will improve the imaging performance and be beneficial to the development of the OCT community.

Index Terms: Optical coherence tomography (OCT), coherent imaging, biophotonics instrumentation, medical photonics instrumentation.

1. Introduction

Optical coherence tomography (OCT) is a three-dimensional (3D) imaging technique that can provide non-invasive, high-speed, and high-resolution images of scattering media and has been applied in the field of medicine and biology [1]–[7]. In Fourier domain OCT (FD-OCT), the transverse resolution is determined by the diffraction-limited spot size of the sample focusing beam, and the depth of focus (DOF) is defined as a confocal parameter and is proportional to the square of the transverse resolution. Consequently, a higher transverse resolution inevitably results in a shorter DOF. When a high numerical aperture (NA) focusing lens is typically used in an OCT system, which will inevitably result in a high transverse resolution but a limited DOF. As high resolution imaging is highly desired in tissues imaging, various approaches have been reported to achieve extended DOF while employing a high NA focusing lens, such as Bessel beams [2], or digital refocusing [8], [9]. Although these methods can achieve transverse superresolution or extend DOF, they suffer from long acquisition times, sensitivity loss, heavy computational costs, and complex system configurations. To solve the trade-off of transverse resolution and DOF, a super-resolution technique, termed pixel reassignment (PRA) [10]–[13], has been applied to OCT system with

an extended DOF and improved detection intensity. PRA has been well studied in the field of confocal scanning microscopy (CSM) and structured illumination microscopy (SIM) [10], [14], [15]. In principle, CSM can improve upon the classical diffraction-limited resolution by a factor of $\sqrt{2}$. Unfortunately, the pinhole is usually reduced to obtain this theoretical resolution enhancement, which results in a heavy reduction in the detection intensity. SIM can obtain resolution enhancement without reducing the detection intensity but with increased hardware complexity and acquisition time. PRA achieves superresolution by reassigning the detected photons to a position halfway between the nominal excitation and detection positions in microscopy.

In this paper, a pixel-reassigned spectral domain OCT (SD-OCT) system was constructed to break the diffraction limitation and obtain an extended DOF and enhanced intensity as well. Numerical simulations and imaging experiments were conducted to characterize the performance of PRA. The experimental results agreed well with the numerical simulations, which verified the feasibility of OCT to improve the overall imaging performance.

2. Pixel Reassignment

Here, we begin with a discussion of mechanism of PRA in a standard CSM. The system intensity point spread function (PSF) of a standard CSM [10], [11], [13] is defined as the product of the illumination and detection intensity PSFs, where the latter is convolved with the pinhole function:

$$h_{sys}(x, y, z) = h_{ill}(x, y, z) \cdot [h_{ill}(x, y, z) * p(x, y)] \tag{1}$$

where $h_{ill}(x, y, z)$ and $h_{ill}(x, y, z)$ are the intensities of the electrical field distribution of illumination and detection light, respectively. $p(x, y)$ is the aperture function defining the pinhole size and shape, $*$ represents the two-dimensional (2D) convolution operation, and x and y denote the variables on the plane perpendicular to the optical z axis. Theoretically, CSM allows the diffraction-limited transverse resolution to be enhanced by a factor of $\sqrt{2}$, which can only practically be obtained with a closed pinhole. Generally, this resolution enhancement is sacrificed to obtain a higher intensity.

If we assume a Gaussian distribution, $f(x, y) = exp[\frac{-(x^2+y^2)}{2\sigma^2}]$ (where σ is the standard deviation), for the illumination and detection intensity PSFs, then the system intensity PSF is found to have the standard deviation as described in [12]:

$$\sigma_{sys}^2 = (1 - m)^2\sigma_{ill}^2 + m^2\sigma_{det}^2 \tag{2}$$

where $m \in [0, 1]$ is the ratio of the off-axis distance of the illumination and detection intensity PSFs. Because Stokes shift is not considered ($\sigma_{ill}^2 = \sigma_{det}^2 = \sigma^2$) in an OCT system, σ_{sys} achieves its minimum value $\sigma_{sys} = \frac{\sigma}{\sqrt{2}}$ when $m = 0.5$. Practically, by reassigning the detected photons to a position halfway between the nominal illumination and detection PSFs and then summing them together, PRA achieves a transverse resolution improvement factor of $\sqrt{2}$ accompanied by enhanced intensity.

3. Numerical Analysis

We performed numerical simulations using MATLAB software (MathWorks, Natick, MA, USA) to characterize PSFs and coherence transfer functions (CTFs) of the PRA technique. The CTF is the Fourier transform of the effective PSF and can describe the image formation in an OCT system [16], [17]. Here, we consider an on-axis aperture and five off-axis detection apertures, which are defined by the detection fibers (Fig. 1(a)). Gaussian illumination is assumed. We define the radius of the full aperture as 1, and the detection fibers are transversely shifted by a step of 0.1; the full-width-at-half-maximum (FWHM) of detected PSFs becomes sharper and is accompanied by decreased intensity (Fig. 1(b)). When all five off-axis PSFs are shifted to the center of the detection aperture and added together, a 1.6 times higher and 1.5 times sharper PSF arises (Fig. 1(b)), which means that PRA results in superresolution with higher detection efficiency than those of standard OCT. This is also demonstrated by the fact that the CTF of PRA has a wider range of relative spatial frequency and detection efficiency than those of standard OCT (Fig. 1(c)).

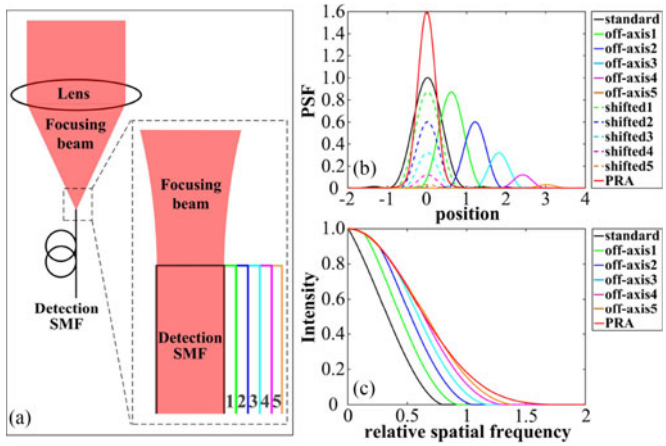

Fig. 1. Optics model and numerical simulation results. (a) Optics model of the simulation. The detection fibers are transversely shifted to five off-axis positions indicated by 1–5. (b) Simulated PSFs of standard detection (black solid line), off-axis detection (green, blue, cyan, magenta, and orange solid lines), off-axis detection shifted to the center (green, blue, cyan, magenta, and orange dashed lines) and PRA detection (red solid line). (c) Simulated CTFs of standard detection (black solid line), off-axis detection (green, blue, cyan, magenta, and yellow solid lines) and PRA detection (red solid line). SMF, single mode fiber.

In SD-OCT, the detected interference signal in *k*-space, including the direct current (DC) term, cross-correlation (CC) term, and auto-correlation (AC) term, is given by

$$I(k) = S(k)\left[DC + 2\int_{-\infty}^{+\infty} a(z)\cos(2knz + \phi)dz + AC\right] \tag{3}$$

where $S(k)$ is the spectral intensity distribution of the light source, $a(z)$ is the amplitude of the elementary waves versus depth. n is the refractive index of the scattering sample. ϕ is the phase shift of the interferometric signal. The DC and AC terms are omitted in the following derivation for simplification. In the experiments, we transversely shift the detection fiber and detect multiple cross-sectional images (B-scans, $B(x, y)$); thus, the PRA process consists of two main steps: 1) transverse shifting, to shift multiple B-scans to the on-axis position of the detection fiber, and 2) summation, to sum multiple B-scans to realize PRA. First, all B-scans are shifted to the on-axis position, and the m-th ($m \in [1, N]$) B-scan is given by

$$B_m^{sh} = B_m(x + \delta, y) \tag{4}$$

where N represents the total number of B-scans. The superscript sh represents the transverse shifting operation, and δ represents the transverse shifting distance. Second, all B-scans are summed together to realize PRA. The resulting B-scan is given by

$$B_{PRA}(x, y) = \sum_{m=1}^{N} B_m^{sh}(x, y) \tag{5}$$

By simply adding a stepper motor to transversely shift the detection fiber without increasing the system complexity, this PRA achieves transverse superresolution and enhanced intensity.

4. Experimental Methods

In the constructed fiber-based SD-OCT system with pixel reassignment shown in Fig. 2, light from a supercontinuum source (SuperK Extreme OCT, NKT Photonics A/C, Birkerod, Denmark) is filtered by a dichroic mirror (DMSP950, Thorlabs, Newton, NJ, USA), resulting in a center wavelength of 890 nm and a 3-dB bandwidth of 180 nm. A 2×2 coupler OC1 (TW850R2A2, Thorlabs, Newton, NJ, USA) is used to separate the input beam into beams

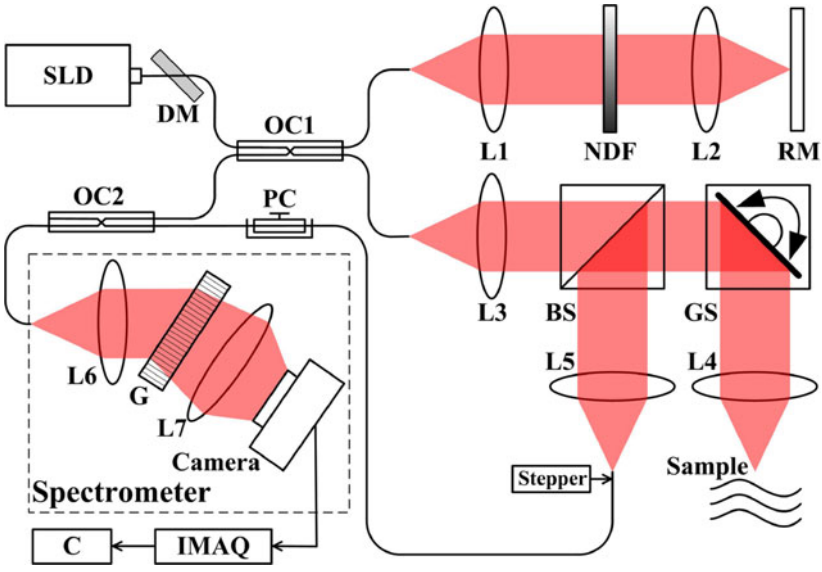

Fig. 2. Schematic of the SD-OCT system with pixel reassignment. SLD, super luminescent diode; DM, dichroic mirror; OC1-2, 90:10 fiber optic coupler; L1-6, lens; L7, camera lens; NDF, neutral density filter; RM, reference mirror; BS, beam splitter; GS, two-dimensional galvo scanner; G, transmission diffraction grating; IMAQ, image acquisition; C, computer; Stepper, stepper motor actuator; PC, polarization controller; SMF, single mode fiber.

of the reference (10%) and sample (90%) arms. The reference arm consists of a collimation lens L1 (AC050-010-B-ML, Thorlabs, Newton, NJ, USA), a neutral density filter NDF (NDL-10C-4, Thorlabs, Newton, NJ, USA), an objective lens L2 (NA $=$ 0.42, M Plan Apo NIR 20, Mitutoyo, Takatsu-ku, Kawasaki, JP), and a reference mirror RM (PF10-03-P01, Thorlabs, Newton, NJ, USA). The sample arm consists of a collimation lens L3 (AC050-010-B-ML, Thorlabs, Newton, NJ, USA), a galvo scanner (GVS002, Thorlabs, Newton, NJ, USA), and an objective lens L4 (NA $=$ 0.42, M Plan Apo NIR 20, Mitutoyo, Takatsu-ku, Kawasaki, JP). A 50:50 beam splitter (BS017, Thorlabs, Newton, NJ, USA) is inserted into the sample arm to build up a dark-field apparatus. The backscattered light from the sample is focused by an L5 lens (AC050-010-B-ML, Thorlabs, Newton, NJ, USA), guided to the other 2×2 coupler OC2 (TW850R2A2, Thorlabs, Newton, NJ, USA), recombined with the reflected light from the reference arm, and finally directed into the spectrometer after being collimated by an L6 lens (AC254-040-B-ML, Thorlabs, Newton, NJ, USA). The spectrometer consists of a 1500 lines/mm diffraction grating (PING-1500/915-980-030, Ibsen Photonics, Farum, Denmark), a camera lens (85 mm, f/1.2, Canon, Tokyo, JP), and a 4096-pixel CCD camera (AViiVA EM4, e2V, Chelmsford, UK). The detected spectrum is digitized at 12-bit resolution and transferred to a computer via an image acquisition board (KBN-PCE-CL4-F, Bitflow, Woburn, MA, USA). Both the camera and the galvo scanner are synchronized by the external trigger from a data acquisition (DAQ) board (PCI-6221, National Instruments, Austin, TX, USA). Discrete Fourier transform is performed on each frame of 1024 axial-lines (A-lines) to resolve the axial depth profile of the sample. To implement superresolution using PRA, a stepper motor actuator (ZFS06, Thorlabs, Newton, NJ, USA) is inserted into the sample arm and linearly shifts the detection fiber along a transverse direction perpendicular to the optical axis. The B-scans are captured after each step of the transverse shifting of the detection fiber. All B-scans captured from the off-axis detection fiber are summed to give a transverse superresolution and an extended DOF.

5. Experimental Results

High transverse resolution can only be achieved within DOF, beyond which the focusing beam diverges quickly and the intensity and transverse resolution deteriorates greatly. To demonstrate

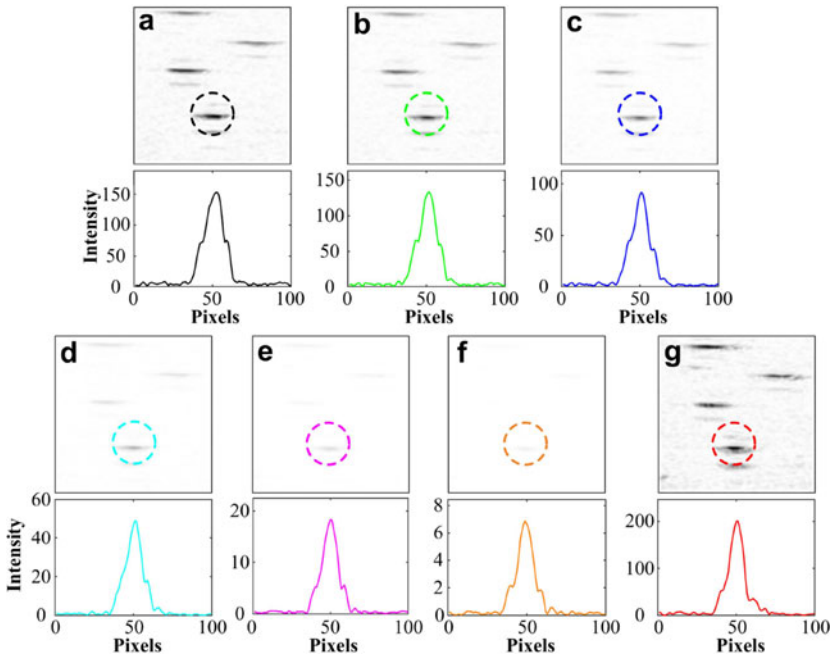

Fig. 3. PRA process. Selected sections of B-scans and transverse profiles of the microparticles captured by the (a) on-axis and (b–f) off-axis detection fibers. (g) Selected sections of B-scans and transverse profiles of the microparticles after PRA. B-scans consist of 100 (axial) $\times$ 100 (transverse) pixels covering 85.16 $\times$ 85.16 μm.

the super-resolving performance using PRA, we conducted the imaging experiments using the phantom of polystyrene calibration microparticles, which was constructed by mixing the agarose solution (No. PC0701-100g, Vivantis, Oceanside CA, USA) with polystyrene microparticles (No. 64090-15, nominal size 6 μm, Sigma-Aldrich, St. Louis, Missouri, USA). This mixture was stored in a vial and placed in an ultrasonic bath for 10 minutes to remove residual clusters. The sample (10 grams) was poured into a cell culture dish, cured for 30 minutes at 100 $^{\circ}$C and then cured for 24 hours at room temperature. Fig. 3 shows the process of PRA. Fig. 3(a) is the original B-scan captured with the detection fiber on-axis. Fig. 3(b)–(f) are five B-scans acquired when the detection fiber was transversely shifted to five off-axis positions with a step of 2 μm. Fig. 3(g) is the pixel-reassigned B-scan. All of the corresponding transverse profiles of the selected microparticle are presented below the B-scans. The detected FWHM of the transverse profiles from Fig. 3(a)–(f) are 13.33, 11.96, 11.82, 11.24, 10.96, and 10.85 pixels, respectively. When the off-axis distance of the detection fiber increases step by step, the value of the detected intensity decreases from 153 to 7 and the FWHM of the transverse profiles decreases from 13.3 to 10.85 pixels. The pixel reassignment operation gives a sharper FWHM of 10.03 pixels and a higher intensity value of 199. So the transverse FWHM and detected intensity are both enhanced by 1.31 and 1.30 times, respectively, compared to those of the standard SD-OCT without PRA (Fig. 3(a)).

Fig. 4(a) reveals that the original B-scan captured with the detection fiber on-axis suffered from defocusing beyond the DOF and then is compensated using the spectral estimation algorithm [8]. Fig. 4(b) presents the resulting B-scan after PRA. The PRA process consists of two steps corresponding to Eqs. (4) and (5). First, five B-scans are captured after each step of the transverse shifting of the detection fiber. Second, all five off-axis B-scans are transversely shifted to the on-axis position of the detection fiber and are then summed. By comparing Fig. 4(a) to 4(b), the transverse super-resolving performance of PRA can be intuitively demonstrated. PRA can be intuitively demonstrated. PRA can be intuitively demonstrated.

Fig. 5 shows the analysis of the transverse FWHM and DOF of the microparticles in Fig. 4. The scatter plots in Fig. 5(a) and (b) indicate the transverse FWHMs as a function of the axial depth.

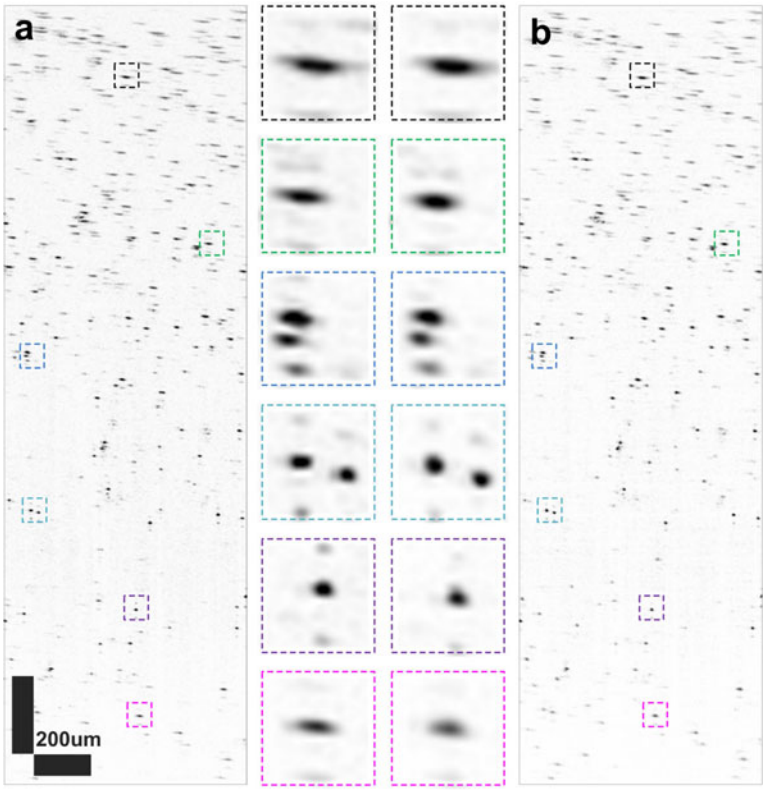

Fig. 4. Super-resolving performance of PRA. (a) Dispersion-compensated B-scan. (b) Resulting B-scan after PRA. Inset: magnified views of six calibration microparticles at different depths in (a) and (b) are indicated by the dashed boxes in multiple colors. PRA has transversely super-resolved the microparticles. Both B-scans are normalized by their maximum values and presented in linear scale. The shifting step of the stepper motor is 2 μm.

The red curves indicate the 6-order polynomial fitting of the transverse FWHMs. Because the mode field diameter (MFD, defined by the 1/*e* field) is 5.0 $\pm$ 0.5 μm, the theoretical transverse FWHM of the PSF at focus is estimated to be 2.92 μm at a wavelength of 850 nm. The finest fitted transverse FWHMs of the microparticles in Fig. 5(a) and (b) are 9.08 μm and 8.04 μm; thus, the finest nominal transverse FWHMs of the PSFs are 3.08 μm and 2.04 μm, respectively. The transverse resolution at the focus is enhanced by 1.51 times. The dashed black lines indicate the DOF range, defined by the confocal parameter *b*, where the transverse resolution is expanded by $\sqrt{2}$ times. The transverse FWHM at the depth is 10.36 μm, corresponding to DOFs of 201 μm and 270 μm in Fig. 4(a) and (b), respectively. The DOF is extended by 1.34 times. The scatter plots in Fig. 5(c) and (d) indicate the intensity distribution as a function of the axial depth. The red curves indicate the 6-order polynomial fitting of the intensity distribution. The dashed black lines show that they had nearly the same 3-dB imaging depth range. The highest fitted intensities of the microparticles in Fig. 4(c) and (d) are $-$11.10 dB and $-$9.34 dB, respectively. The intensity is improved by 1.76 dB, which is equal to 1.50 times.

6. Discussions and Conclusions

In conclusion, we have developed a pixel-reassigned SD-OCT system for transverse superresolution. The numerical simulation and imaging experiments of microparticles demonstrate an advantage of PRA that the transverse resolution, DOF, and intensity are moderately improved at the same time. However, the current pixel-reassigned SD-OCT is implemented at the cost of imaging

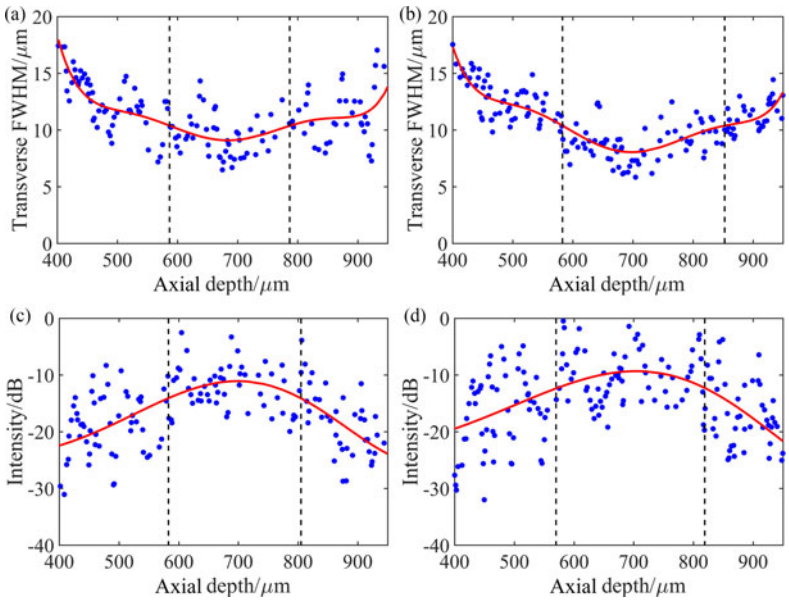

Fig. 5. Analysis of the microparticles. FWHMs along the axial depth in (a) the B-scan of the standard OCT and (b) the B-scan after PRA. The scatter plots indicate the transverse FWHMs as a function of the axial depth. Intensity distribution along the axial depth in (c) the B-scan of the standard OCT and (d) the B-scan after PRA.

speed. In this work, we sum five B-scans corresponding to five distinct off-axis positions of the detection fibers, which decreases the imaging speed by five times. This limitation may be mitigated by reducing transverse shifting steps. As the breaking of diffraction limitation is obtained by recombining the spatial spectra of the detected signals with different off-axis distances. We may reduce the number of shifting steps and increase the distance of each shifting step, so the off-axis steps may even be reduced to two steps. This speed limitation may be also mitigated by the use of faster spectrometers (Cobra-S 800, e2V, Chelmsford, UK) or an ultra-high-speed swept source [18] as well. The proposed PRA apparatus is applicable to desktop OCT imaging systems and improves the overall performance of transverse superresolution, DOF, and intensity.

References

[1] J. G. Fujimoto *et al.*, "Optical biopsy and imaging using optical coherence tomography," *Nature Med.*, vol. 1, no. 9, pp. 970–972, 1995.
[2] L. Liu *et al.*, "Imaging the subcellular structure of human coronary atherosclerosis using micro-optical coherence tomography," *Nature Med.*, vol. 17, no. 8, pp. 1010–1014, 2011.
[3] B. J. Vakoc, D. Fukumura, R. K. Jain, and B. E. Bouma, "Cancer imaging by optical coherence tomography: Preclinical progress and clinical potential," *Nature Rev. Cancer*, vol. 12, no. 5, pp. 363–368, 2012.
[4] J. Ha *et al.*, "Compensation of motion artifacts in catheter-based optical frequency domain imaging," *Opt. Exp.*, vol. 18, no. 11, pp. 11418–11427, 2010.
[5] E. Bo, X. Liu, S. Chen, X. Yu, X. Wang, and L. Liu, "Spectral-domain optical coherence tomography with dual-balanced detection for auto-correlation artifacts reduction," *Opt. Exp.*, vol. 23, no. 21, pp. 28050–28058, 2015.
[6] B. A. Standish *et al.*, "In vivo endoscopic multi-beam optical coherence tomography," *Phys. Med. Biol.*, vol. 55, no. 3, p. 615, 2010.
[7] E. Bo *et al.*, "Single-camera full-range high-resolution spectral domain optical coherence tomography," *Appl. Opt.*, vol. 56, no. 3, pp. 470–475, 2017.
[8] E. Bo *et al.*, "Depth-of-focus extension in optical coherence tomography via multiple aperture synthesis," *Optica*, vol. 4, no. 7, pp. 701–706, 2017.
[9] E. Bo *et al.*, "Multiple aperture synthetic optical coherence tomography for biological tissue imaging," *Opt. Exp.*, vol. 26, no. 2, pp. 772–780, 2018.
[10] C. Sheppard, "Super-resolution in confocal imaging," *Optik*, vol. 80, no. 2, pp. 53–54, 1988.
[11] C. J. Sheppard, S. B. Mehta, and R. Heintzmann, "Superresolution by image scanning microscopy using pixel reassignment," *Opt. Lett.*, vol. 38, no. 15, pp. 2889–2892, 2013.

[12] S. Roth, C. J. Sheppard, K. Wicker, and R. Heintzmann, "Optical photon reassignment microscopy (OPRA)," *Opt. Nanoscopy*, vol. 2, no. 1, pp. 1–6, 2013.
[13] M. Castello, C. J. Sheppard, A. Diaspro, and G. Vicidomini, "Image scanning microscopy with a quadrant detector," *Opt. Lett.*, vol. 40, no. 22, pp. 5355–5358, 2015.
[14] L. Liu, N. Chen, and C. Sheppard, "Double-reflection polygon mirror for high-speed optical coherence microscopy," *Opt. Lett.*, vol. 32, no. 24, pp. 3528–3530, 2007.
[15] B. Wang, R. Lu, Q. Zhang, and X. Yao, "Breaking diffraction limit of lateral resolution in optical coherence tomography," *Quantitative Imag. Med. Surg.*, vol. 3, no. 5, pp. 243–248, 2013.
[16] M. Gu, X. Gan, and C. Sheppard, "Three-dimensional coherent transfer functions in fiber-optical confocal scanning microscopes," *JOSA A*, vol. 8, no. 7, pp. 1019–1025, 1991.
[17] M. Gu and C. Sheppard, "Three-dimensional optical transfer function in a fiber-optical confocal fluorescence microscope using annular lenses," *JOSA A*, vol. 9, no. 11, pp. 1991–1999, 1992.
[18] Y. Ling, X. Yao, and C. P. Hendon, "Highly phase-stable 200 kHz swept-source optical coherence tomography based on KTN electro-optic deflector," *Biomed. Opt. Exp.*, vol. 8, no. 8, pp. 3687–3699, 2017.